Journal of Applied Physics ARTICLE scitation.org/journal/jap

Nondestructive microstructural investigation of defects in 4H-SiC epilayers using a multiscale luminescence analysis approach

Cite as: J. Appl. Phys. **131**, 185705 (2022); doi: 10.1063/5.0088313
Submitted: 15 February 2022 · Accepted: 23 April 2022 ·
Published Online: 12 May 2022

Sami A. El Hageali,[1,2,a)] Harvey Guthrey,[2] Steven Johnston,[2] Jake Soto,[3] Bruce Odekirk,[3] Brian P. Gorman,[1] and Mowafak Al-Jassim[2]

AFFILIATIONS

[1]Colorado School of Mines, 1500 Illinois Street, Golden, Colorado 80401, USA
[2]National Renewable Energy Laboratory, 15013 Denver West Parkway, Golden, Colorado 80401, USA
[3]Microchip Technology Inc., 405 SW Columbia Street, Bend, Oregon 97702, USA

[a)]**Author to whom correspondence should be addressed:** elhageali@mines.edu

ABSTRACT

The development of metal oxide semiconductor field effect transistors (MOSFETs) utilizing epitaxially grown 4H-SiC has accelerated in recent years due to their favorable properties, including a high breakdown field, high saturated electron drift velocity, and good thermal conductivity. However, extended defects in epitaxial 4H-SiC can affect both device yields and operational lifetime. In this work, we demonstrate the importance of a multiscale luminescence characterization approach to studying nondestructively extended defects in epitaxial 4H-SiC semiconducting materials. Multiscale luminescence analysis reveals different aspects of excess charge carrier recombination behavior based on the scale of a particular measurement. Combining measurements of the same extended defect area at different scales tells us more about the essential nature of that defect and its microstructure. Here, we use photoluminescence imaging and cathodoluminescence spectrum imaging to investigate the recombination behavior of several different types of extended defects, including stacking faults, inclusions, and basal plane dislocations. A detailed understanding of the optoelectronic properties of extended defects in epitaxial SiC helps elucidate the microstructure of extended defects and can provide pathways to mitigate detrimental changes during device operation related to their evolution, such as the recombination enhanced dislocation glide effect that affects SiC-based MOSFETs.

I. INTRODUCTION

Silicon carbide (SiC) possesses superior electrical and thermal properties compared to silicon, including a high breakdown field, high saturated electron drift velocity, good thermal conductivity, and other critical advantages, as described by Tamaso *et al.*[1] For example, compared to silicon, the breakdown field of 4H-SiC is ten times larger, the saturated electron drift velocity is twice as fast, and the thermal conductivity is about three times larger.[2,1] These properties make wide bandgap materials ideal for applications in high-frequency and high-power electronic devices, particularly because they are resistant in harsh environments.[3] SiC plays an important role in the microelectronics industry due to these outstanding physical properties and the availability of commercial wafers up to 8 in. However, one limitation is the occurrence of extended defects in the epitaxial layer, which result in unpropitious effects on devices. These defects are often found to propagate from the substrate or epilayer/substrate interface.

In truth, SiC materials often exhibit relatively high defect density, which may primarily affect reliability and may decrease device yield. The typical densities of threading screw dislocations, threading edge dislocations, and basal plane dislocations (BPDs) in commercial 4H-SiC substrates can be 10^2–10^3, 10^3–10^4, and 10^2–10^4 cm^{-2}, respectively.[4] This does not account for the 2D defects (e.g., planar stacking faults) generated from these dislocations nor the 3D defects (e.g., epi-pyramids and inclusions) in the epilayer. Thus, even though very high voltage bipolar devices and metal oxide semiconductor field effect transistors (MOSFETs) are

readily available on the market, their potential has not been fully reached. Indeed, it has been demonstrated that a forward bias on a p-n junction can induce the formation and motion of a single Shockley-type stacking fault (SF) through a BPD via an effect called recombination enhanced dislocation glide (REDG).[5] This effect can result in the rapid propagation of the fault and accentuate degradation behavior in electrical properties resulting in failure. Because the SFs in 4H-SiC act as quantum wells, the generation of SFs decreases the lifetime and consequently increases the reverse-bias leakage current. This phenomenon is called forward voltage drift (FVD), and it degrades bipolar devices during their operation.[6]

3C-inclusions, also known as down-falls, are one of the main device-killing defects (among others, such as foreign polytypes, micropipes, and BPDs) in 4H-SiC drift layers and are well known in the SiC community. In current state-of-the-art wafers, this defect is present in almost if not all epitaxially grown 4H-SiC wafers. The density of this defect is particularly high around the edges of the wafer and tends to decrease toward the center of the wafer due to its origin. Indeed, these inclusions are known to be induced by surface contaminants, such as particles, that deposit onto the substrate surface during the initial stages of growth.[7] However, the nature of the particle is still unclear. While some suggest that these down-fall particles are polycrystalline 3C-SiC deposits,[8] others argue that they are Si clusters that form in the gas phase for silane-propane based CVD during the epi-growth when growth rate conditions are exceeded.[9,10] Without excluding the possibility of other nucleation mechanisms nowadays, in state-of-the-art epitaxially grown layers, growth conditions are established and it is found that 3C-inclusions nucleate from SiC particulates falling down from the inner walls of the reactor or via pre-handling of the wafer.[10] These particulates are present in abundance on the wafer support and proper handling of the wafer is critical to avoid contamination of the wafer majoritarily on the edges where their density is found to be the highest.[11] Regarding the formation of the inclusion, a high local supersaturation on the substrate surface results in the spontaneous nucleation of 3C. This 2D nucleation affects the growth of the step flow and is, therefore, a major source of BPDs during epitaxial growth, due to the strain generated around the particle. The lattice mismatch between the particle and the 4H-SiC substrate causes zones of compressive and tensile stress within the epitaxial material during growth, which is relaxed via BPD generation, thereby generating a misoriented 4H-SiC.

Down-falls are of particular concern because they have not only been reported to reduce the blocking voltage of SiC p-n diodes, but they also lead to degradation issues in unipolar devices in which the body diode is forward biased, such as MOSFETs. The inclusion itself causes reverse leakage, voltage breakdown reduction, increased on-state resistance, and threshold voltage drift due to degradation of the SiC surface, traps in oxide, and other factors. The considerable number of BPDs generated in this defect area is a leading source of degradation. Specifically, the expanding SFs degrade the drift conductivity by radically diminishing carrier lifetime and introducing barriers known as traps in the forbidden gap. BPDs and SFs due to inclusions are different from BPDs coming from substrates. They are more severe, and the inclusion is mostly a total killer defect (i.e., it results in die failure). These SFs that expand from the BPDs gradually increase the differential negative resistance and degrade the breakdown voltage.[12]

Photoluminescence (PL) and electroluminescence (EL) imaging analysis are commonly used to show these inclusions, using a long-pass filter (>700 nm) to reveal BPDs. However, due to the total size of the extended defects, these measurements are typically presented at the mm and sub-mm scales, without a thorough luminescence analysis of the area at the microscale. Down-falls usually result in a multiple SF area due to the change in the surface morphology induced by the strain energy; the down-falls form large (0001+ off-cut angle) surface terraces.[13] In the past, cathodoluminescence (CL) has been proven to be a useful characterization tool for the identification of SFs at the macroscale.[14,15]

Reducing the defect density in epilayers is essential for fabricating SiC devices, but a thorough understanding and detailed analysis of the defects, from the macroscale to the microscale, is also important. Such an analysis allows us to directly correlate the nature of the defect to its impact during device operation (FVD phenomena) and the effect of the REDG mechanism. Indeed, the industrial development of SiC devices gets into the deep learning phase where the necessity of sorting out devices by their electrical yield at the production end becomes crucial. Identification of the nature of defects can be correlated to crucial device degradation parameters such as leakage current, breakdown voltage, maximum voltage between drain-to-source (V_{DS}), maximum voltage between gate-to-source (V_{GS}), drain current (I_D), and the REDG degradation. In this work, we introduce a multiscale luminescence analysis that helps provides pathways to understand precisely the effect of specific types of defects on the electrical performance of the devices. In turn, this knowledge allows us to fulfill the potential advantages that 4H-SiC has to offer. This multiscale luminescence characterization approach, using PL imaging and cathodoluminescence spectrum imaging (CLSI), can allow us to investigate the microstructure of an extended defect and provide a more detailed understanding of its optoelectronic properties.

II. EXPERIMENTAL

The specimen used in this study has a CVD grown 30-μm-thick 4H-SiC epitaxial layer and is lightly n-type doped ($Nd = 3 \times 10^{15}$ cm^{-3}). The epilayer was grown on 4H-SiC n-type conductive substrate with an off-cut angle of 4°. The growth conditions are unknown, but this specimen is representative of state-of-the-art available commercial wafers on the market. We used a Princeton Instruments PIXIS 1024BR Si-charge-coupled device (CCD) camera for band-to-band PL imaging. The camera was cooled to −60 °C to reduce background counts, and the total background and readout noise was only about 1% of the 16-bit pixel capacity; thus, no background image was needed for subtraction. The ultraviolet PL (UV-PL) images were collected while the sample was housed in a dark enclosure.

Excitation light was provided by a 360-nm laser diode. An automated filter wheel from Edmund Optics with six positions was used to change the output filters for each acquisition. Each PL image was filtered by a narrow (full width at half maximum <10 nm) bandpass filter at 420, 450, 480, 488, 500, and 550 nm. A long-pass (LP) filter (LP >700 nm) was used to observe BPDs,

which allowed us to see the entire structure of the defect. Image acquisition times can range from seconds to minutes, and for this sample, in particular, exposure times of 3 min and 30 s were adequate to collect the PL images at high and low resolution, respectively, and nearly fill the detector pixels. It is to note that observation and expansion of dislocations can simultaneously occur during UV-PL imaging via the REDG mechanism mentioned above. To minimize the dislocation expansion, we drastically reduced the defect exposure to laser irradiation time by turning it on only when necessary. UV-light was shined on the defect only for acquisition time. Furthermore, optical mirrors are used in front of the laser head and allow to move our laser spot over the entire field of view during acquisition and this provides discontinuous illumination that reduces considerably the expansion velocity of mobile dislocations which becomes near non-existent. Moreover, power density is a critical factor. Hirano *et al.*[16] investigated the effect of light illumination on the REDG mechanism in 4H-SiC by conducting photoluminescence experiments. The results showed that the enhanced rate of a mobile partial dislocation glide is controlled by the effective light intensity at the dislocations rather than by the photoexcited carrier density. This suggests that the glide enhancement is induced by the photoionization of dislocations. Practically, while keeping the photocarrier concentration constant (uniform excitation conditions), the effective power density for the direct excitation of dislocation states is controlled by having a low output light intensity and adequate mirror frequency to scan the beam over the field of view for discontinuous excitation of the dislocations. Thus, it is to be noted that the glide enhancement mechanism is initiated for steady (fixed) and continuous illumination at the specific site of the dislocation. The uncropped images have a resolution of 1024×1024 pixels. For the high spatial resolution PL images, we used a Mitutoyo 20× microscope objective with 0.40 numerical aperture and 20-mm working distance coupled with a Navitar Zoom 6000 lens. The images acquired with this lens system have a field of view (FOV) of $\sim 1.3 \times 1.3\ \text{mm}^2$. For the lower resolution PL images, a Unifoc-12 Schneider macro imaging lens was used, which provides a FOV of $\sim 4 \times 4\ \text{mm}^2$. In general, when using bandpass filters, bright regions [Fig. 1(a)] correspond to strong luminescence emission within the corresponding wavelength range, whereas dark regions indicate the opposite (i.e., no characteristic luminescence in that range). CL measurements were performed on a JEOL JSM-7600F scanning electron microscope using an accelerating voltage of 15 kV and a beam current of ∼3 nA at room temperature (∼298 K) and 8 K. Spectrum-per-pixel data collection was accomplished using a Horiba H-CLUE CL system equipped with a silicon CCD array. These data were processed to produce integrated intensity images, peak emission maps, and CL spectra from different regions of the samples.

III. RESULTS AND DISCUSSION

Figure 1 shows the UV-PL images of the inclusion area acquired with six different output bandpass filters. These images show that only two types of SFs (SF1 and SF2) are emitting in this region. SF1 emitting with the 420 nm bandpass filter [Fig. 1(a)] is likely an extrinsic Frank-type SF or a single Shockley SF, based on the range of wavelength emissions.[6] However, SF2 [the bright SF in Figs. 1(b)–1(e)] seems to have a broad emission, covering the range of 450–500 nm. This may lead to an incorrect identification of this SF. To identify this SF, pixel intensities were evaluated after different efficiency correction factors were applied. This analysis suggested that a triple Shockley SF or an intrinsic Frank-type SF was the most probable option.[6] It is difficult to distinguish between these two SFs due to the similarity in their emission ranges.

Figure 2 shows higher magnification UV-PL images and cropped sections of these images in the inclusion area. Figure 2(a) reveals a considerable dislocation network, both inside and outside the 3C-inclusion. In device operation, glissile dislocations from this network can serve as the origin of SF expansion processes after an extended forward bias operation via the REDG effect. Some of these SFs are already present but cannot be observed due to resolution limits. The UV-PL images in Figs. 2(a)–2(g) show that this BPD network leads to the formation of different SFs inside as well as outside the inclusion. As an example, the V-shaped defects seen in Fig. 2(e), if made of glissile dislocations, can propagate and increase in size. These defects can only be observed using this high-resolution UV-PL image. This is where the multiscale luminescence analysis becomes interesting. Apart from the V-shaped defects, two embedded triangular SFs (TSFs), located next to the tip of the inclusion, are clearly visible in Fig. 2(b). At higher magnification, the UV-PL image in Fig. 2(c) shows two other TSFs emerging from the strain around the tip of the inclusion. One of these TSFs can also be observed when zooming in on the green highlighted area in Fig. 2(g). Multiple other features could also be related to the presence of SFs. If we take a closer look at the brightest side of the inclusion [Fig. 2(d)], the lower part (following the step-flow direction) seems to have been separated from the BPD network, but this is not the case for the dark side [Fig. 2(f)]. This may indicate the presence of SFs on the bright side. The difference between the bright and dark side of the inclusion is discussed later with the CL data.

The SFs that do not emit using our excitation condition reveal their shape through the dislocation network that delineates the SFs. When imaging an inclusion, it is common to acquire an LP >700-nm filtered image to reveal BPDs,[17,18] but these areas typically contain multiple SFs due to the strain generated around the down-fall particle during growth. This could lead to a misidentification of the number and types of SFs present, not only outside the 3C-inclusion, but also inside, which the CL results depict in Figs. 3–5.

Because we are dealing with a 3C-inclusion, we should observe emissions at 550 nm and above, characteristic of the 3C-SiC bulk luminescence emission. However, as mentioned previously, our excitation does not yield a significant amount of this signal, as can be seen with the 550-nm BP filter in Fig. 1(f). The darkest areas are the n3C-SF multilayers (where n indicates the number of layers). When n increases, the luminescence peak position tends to be the same as that of a bulk 3C-SiC material with triangular surface defects. The different layers are shown in the UV-PL image in Fig. 1(b). The SFs, being relatively small and/or having low radiative recombination rates through their defect centers, do not necessarily emit under our excitation conditions; this is the case here when acquiring the UV-PL images at both high and low magnifications. The carrier generation is approximated to $\sim 10^{21}\ \text{cm}^{-3}\,\text{s}^{-1}$ (with a 1-mm laser spot size at

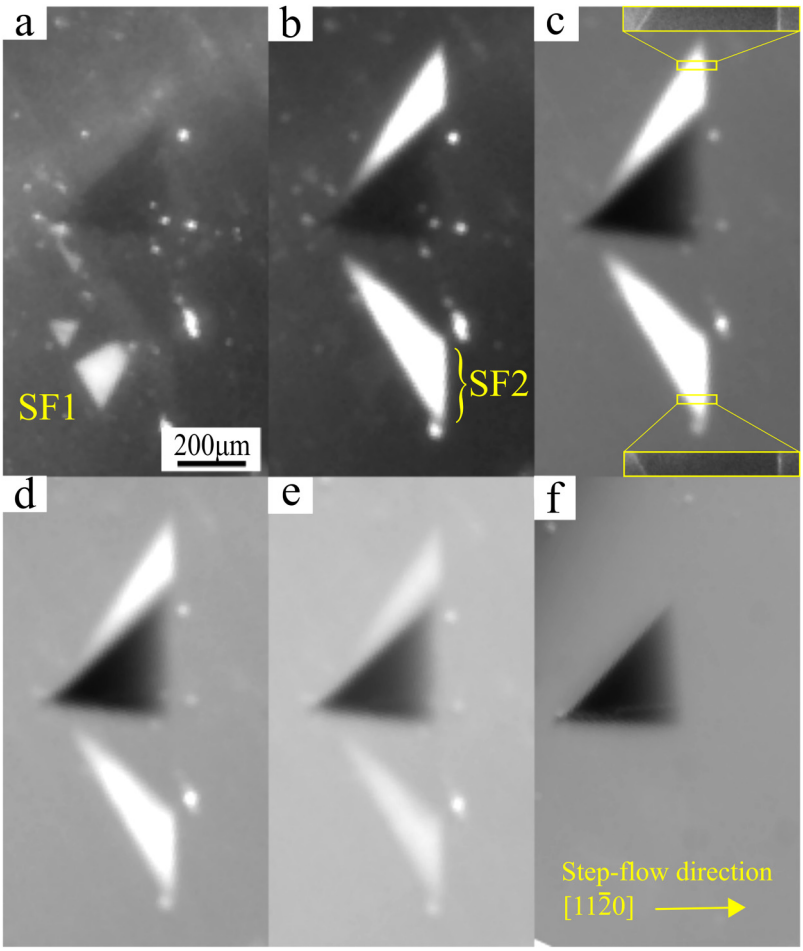

FIG. 1. UV-PL images of the inclusion collected with different output bandpass filters: (a) 420, (b) 450, (c) 480, (d) 488, (e) 500, and (f) 550 nm, with a FWHM of <10 nm. In image (c) are two cropped images (LP >700 nm filter) showing Frank partial dislocations delineating the bright emitting SF.

35 mW) for PL under the experimental conditions used. The same identification process used in Fig. 2 was also done using the high-resolution lens system, but the resulting highlighted regions, shown in Fig. 2, did not yield any useful information about the SFs. In fact, it is very difficult to observe characteristic luminescence emissions from all the SFs in a region of defects, simply because of their different natures, geometries, and behaviors under the same excitation conditions, such as carrier injections, power densities, diffusion lengths, and recombination efficiencies.

Next, we discuss the results of microscale CLSI analysis of this same defect. Figures 3–5 show scanning electron microscope and PL images of the different regions where the CL spectra were acquired. CL peak photon energy maps and spectra corresponding to subregions are also shown. The SFs that had very low emissions under the UV-PL excitation conditions emit more strongly under the CL conditions due to the injection level being several of orders of magnitude higher ($\sim 10^{28}$ cm^{-3} s^{-1}).

The CL measurements for the two first regions (Fig. 3) were done at 298 K for comparison with the UV-PL imaging. The peak photon energy map for region 1 [Fig. 3(c)] shows two distinct local spectra. The emission spectrum in region 1-I corresponds to SF2 present on the side of the inclusion area (identified earlier as either an intrinsic Frank-type SF or a triple Shockley SF). According to the literature, the shape of this peak actually corresponds to an intrinsic Frank-type SF (noted as IFSF in the figures).[19] Indeed, at 298 K, the Frank-type SF has a more pronounced bump (secondary peak) than the triple Shockley SF, for which this secondary peak is barely or not at all apparent (depending on measurement equipment and collection system efficiency).[20] The local emission spectrum from region 1-II corresponds to the TSF (SF1) that merges into the latter SF. It is to note that they are on different basal planes. These TSFs, emitting at 420 nm, are known to be single Shockley SFs (SSSFs). The distinction from the extrinsic Frank-type SF is made thanks to the triangular shape of the SF. The peak photon energy map for region 2 [Fig. 3(d)] also shows two regions with distinct emission spectra. The emission from region 2-I is due to a multilayer n3C-SF emitting at ~550 nm with a secondary peak at ~565 nm and no near-band-edge (NBE) peak is observed. This explains the difference between the bright side and the dark side of the inclusion. In general, the background intensity is made of radiative recombination via defect levels intrinsic to the epilayer and photons with energies outside the filter transmission range that still

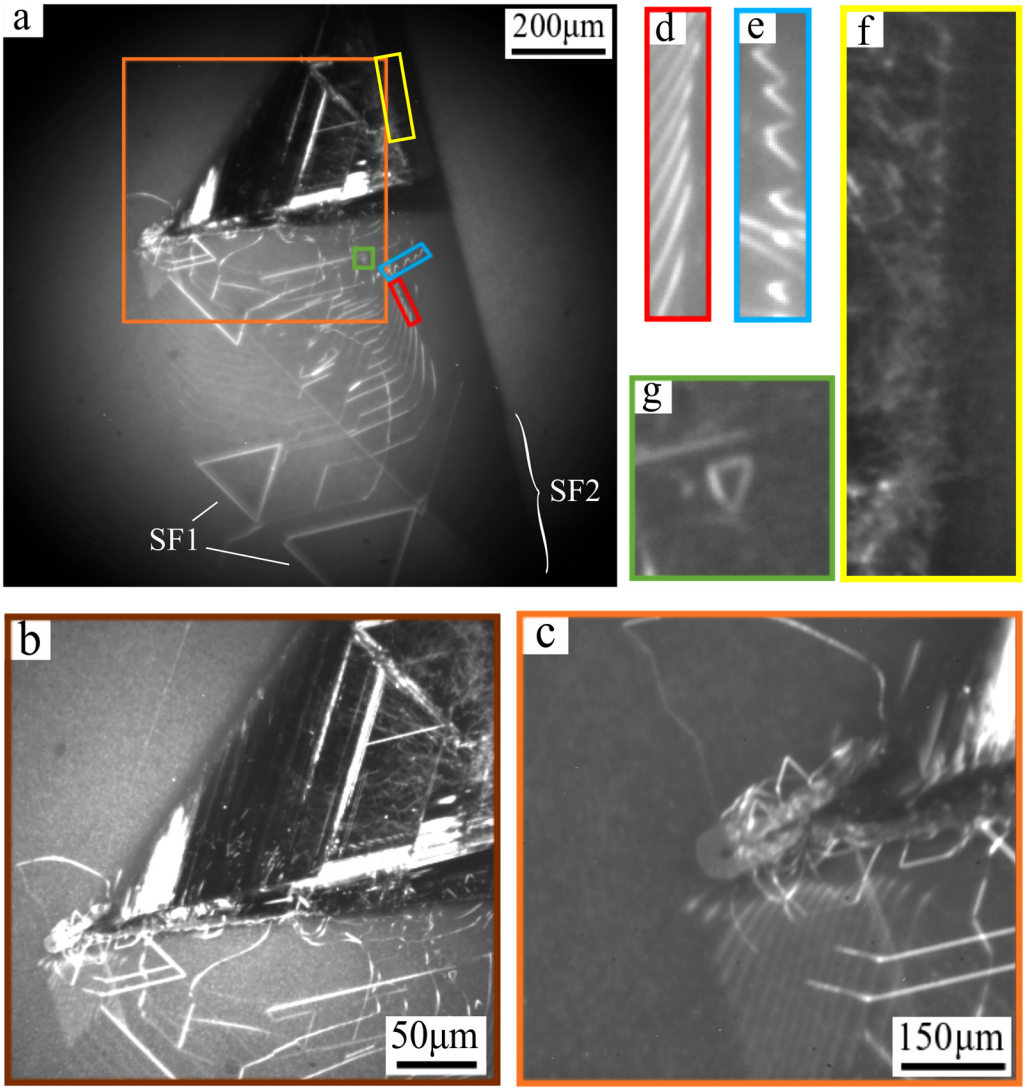

FIG. 2. The UV-PL images [(a)–(c)] were acquired with a LP of >700 nm filter, and the FOV are 1.3, 0.7, and 0.3 mm, respectively. The other images [(d)–(g)] are cropped sections of (a).

transmit through the filters. Consequently, the intensity variation reflects the crystalline quality or defect content of the sample. Thus, the presence of a foreign polytype—in this case, the bulk 3C-SF (dark side)—induces a sudden change in the resulting luminescence signal. Indeed, due to the large number of nonradiative centers induced by dislocations, boundaries, and SFs, the luminescence intensity emission from the 4H-SiC quenches near the bulk 3C, therefore, appears dark in all of the UV-PL images in Fig. 1. Thus, the bulk 3C-SiC can be visualized as dark contrasts on a bright background. The emission in region 2-II corresponds to the same SF as in subregion 1-I, but on the other side of the inclusion area, as shown in Figs. 3(a) and 3(b). These two first regions correlate perfectly with the UV-PL results presented in Fig. 1. Also, in this study, the hypothesis that a Frank-type SF is identified is validated by high-intensity UV illumination. Frank-type SFs are made of sessile dislocations (Frank partials) and, therefore, do not glide under continuous UV excitation, whereas Shockley partials do. The Frank partials delineating the two Frank-type SFs on both sides of the inclusion can be seen in Fig. 2(b) using a long-pass filter of >700 nm to reveal dislocations.

The CL spectra for regions 3 and 4 (Fig. 4) were acquired at T = 80 K to get a stronger signal from the different SFs. The emission from 3-II corresponds to the defect-free region; thus, the band-to-band peak can be seen in the local spectrum. The 3-I

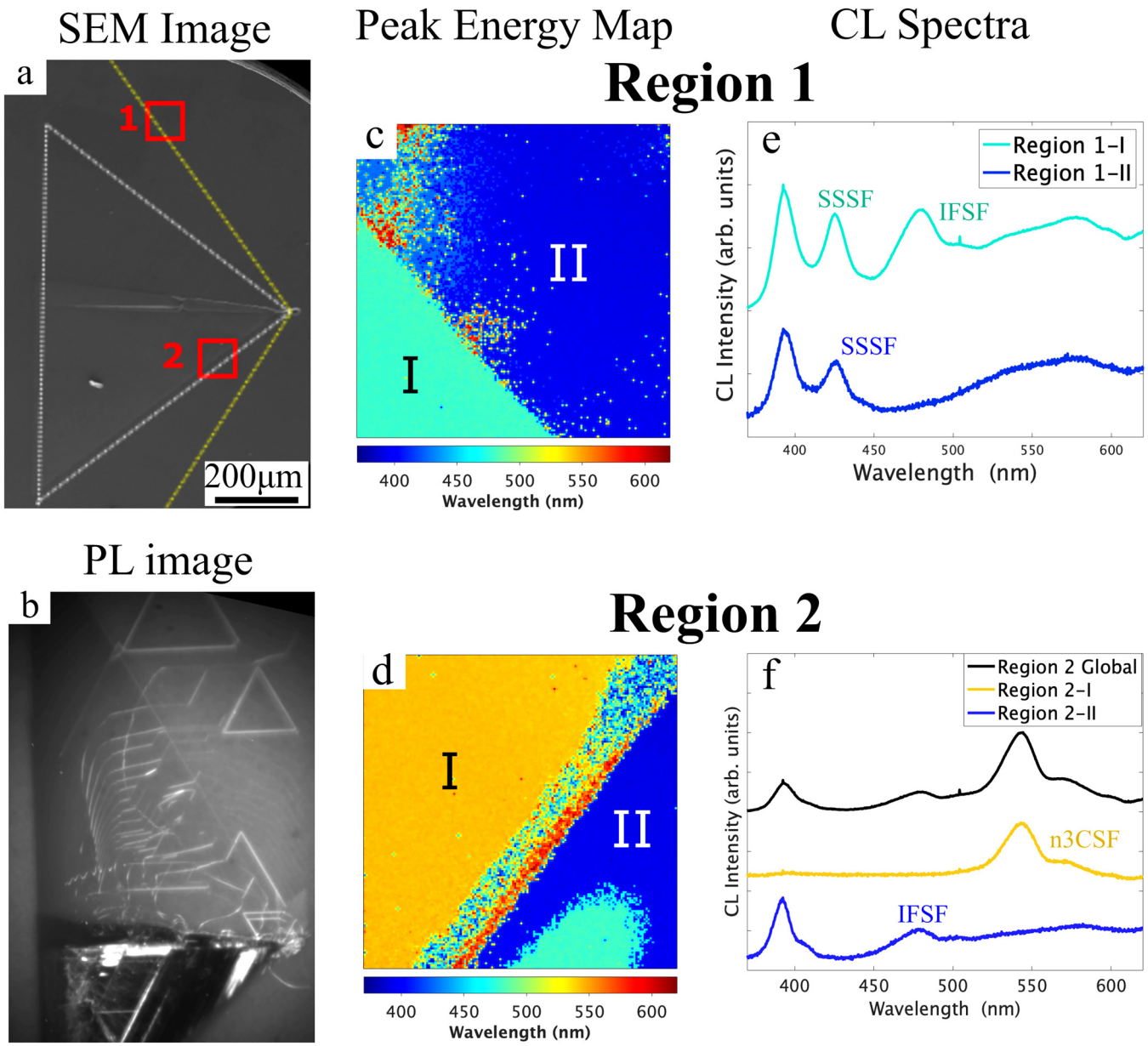

FIG. 3. (a) SEM image, (b) PL image (LP >700 nm), (c) and (d) peak photon energy maps associated with regions 1 and 2, respectively, and (e) and (f) CL spectra at T = 298 K associated with regions 1 and 2, respectively.

emission is characteristic of the same type of SF as in 1-I and 2-II. However, it must be noted that the peak shape from the Frank-type SF was sharper in region 3-I (Fig. 4) than in region 2-II, for two reasons. First, the luminescence peak gradually gets into shape when scanning along the step-flow direction from the substrate/epi-layer interface to the surface substrate, due to the upstream formation of the fault on the basal plane. Second, the spectral acquisition on location 2-II was done at a lower temperature than on 3-I, thus resolving sharper peaks. Region 4 contains the down-fall particle area. We can see that the local spectrum in 4-I shows a peak corresponding to the SSSF observed earlier in the UV-PL images [Fig. 2(c)] around the particle. The region around 4-I would only correspond to a region of high strain, corrupting the crystalline quality of this region and, therefore, showing a noisy background. BPDs would have been detected for a spectral range greater than 600 nm, as can be seen from the UV-PL imaging, given that they

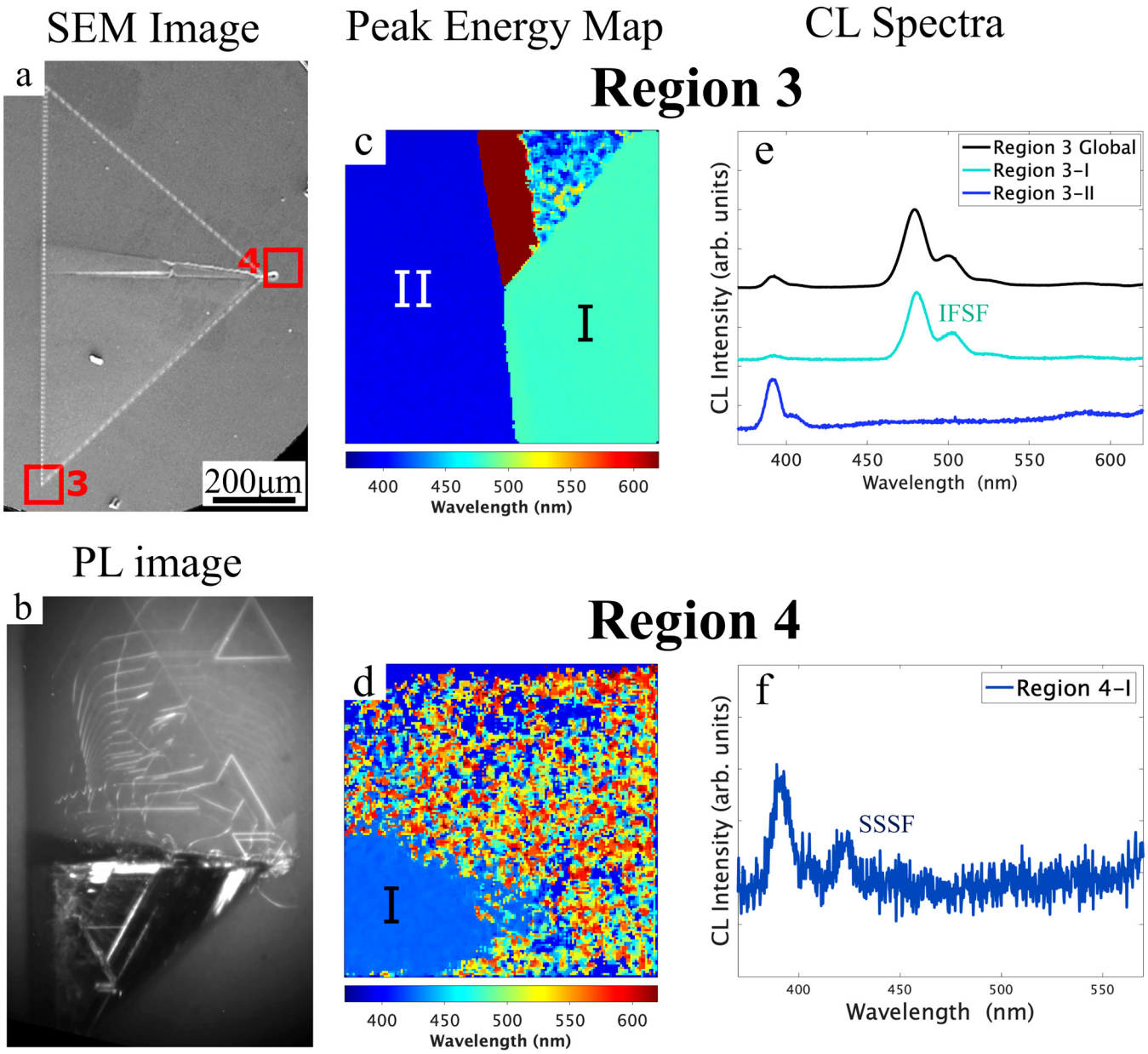

FIG. 4. (a) SEM image, (b) PL image (LP >700 nm), (c) and (d) peak photon energy maps associated with regions 3 and 4, respectively, and (e) and (f) CL spectra at T = 80 K associated with regions 3 and 4, respectively.

have a broad emission range (600–1000 nm).[21] However, the short dwell times for the CLSI acquisition, coupled with the weak emission signal from these BPDs, made it impossible to delineate these features in our analysis.

The peak photon energy maps for regions 5, 6, and 7 (Fig. 5) were acquired at T = 8 K to resolve sharper peaks for the local spectra, as these zones have many sharp features, such as the faceted 3C region in the dark side of the inclusion. The emission spectra from region 5 show peaks from multiple SF features. As mentioned previously, the BPD network seems to have stopped suddenly at the same level on the bright side of the inclusion. We concluded that this may be because of the presence of another structure. The CL data support this reasoning, as they show two distinct subregions. The UV-PL images in Fig. 2 suggest that the

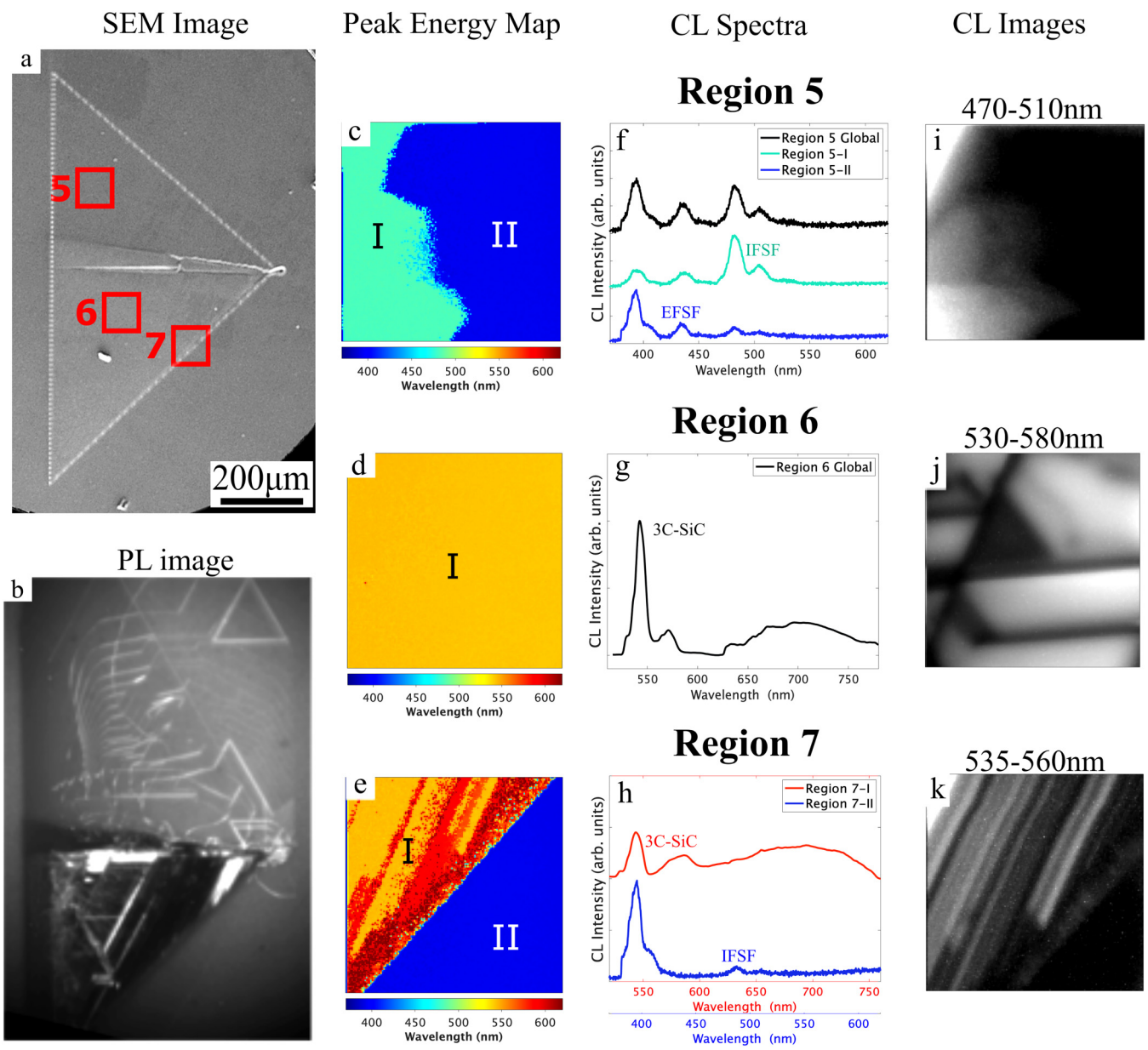

FIG. 5. (a) SEM image, (b) PL image, (c)–(e) peak photon energy maps associated with regions 5, 6, and 7, respectively, (f)–(h) CL spectra at T = 8 K associated with regions 5, 6, and 7, respectively, and (i)–(k) CL images associated with regions 6, 7, and 8, respectively.

shape of the local 5-II spectrum matches that of an extrinsic Frank-type SF [noted as EFSF in Fig. 5(f)]. This SF in 5-II would then convert into an intrinsic Frank-type SF in Fig. 5(i), leading to its local spectrum in 5-I. Additionally, as the CL spectra in Fig. 5(f) suggest, the brighter region is not an entirely different structure; it still shows a band-to-band peak emission (mismatched 4H-SiC with SFs and dislocations lying on the basal plane), unlike the dark side (faceted bulk 3C-SiC) where the 4H-SiC NBE peak is absent, which is why it looks brighter in the UV-PL images in Figs. 1 and 2. This bright region is referred to as misoriented 4H-SiC. The particle at the origin of the inclusion disrupts the growth flow direction, which then, with strain energy, results in a misoriented 4H-SiC layer. The emission from region 6 was acquired away from the edge of the inclusion [Fig. 5(a)]. The CL image in Fig. 5(j) shows the multilayered 3C structure in more detail. A more pronounced peak, corresponding to the

luminescence from the bulk 3C polytype, can be seen because the NBE peak is absent in this region. The corresponding spectrum also shows characteristic luminescence from BPDs above 600 nm.

The peak photon energy map from subregion 7-I [Fig. 5(e)] shows distinctive features corresponding to the faceted 3C-SF layers. Spectrum 7-I [shown in red in Fig. 5(h)] is given with a spectral range of 500–800 nm. It shows a peak corresponding to the 3C-inclusion polytype at 550 nm, as well as a broad emission from ~600 nm to approximately 750 nm that corresponds to luminescence from BPDs. This was expected from the UV-PL imaging that showed the highly multilayered 3C-SF connected via BPDs; this is also pictured in the CL image in Fig. 5(k). In the local spectrum from subregion 7-II [shown in blue in Fig. 5(h); 350–650 nm], the intrinsic Frank-type SF shows up, as anticipated, with a dimmed emission, due to its depth level in the epilayer.

IV. SUMMARY

In summary, we have used multiscale luminescence analysis to show that the BPD network generated from strain around the down-fall particle indicates the presence of different structures, such as Shockley-type and Frank-type SFs. UV-PL imaging allowed for a rapid identification of the inner structure of the defect by revealing the BPD network and the presence of various SFs (Figs. 1 and 2), and CL was used to provide better spatial and spectral information (Figs. 3–5). This work highlights the power of multiscale luminescence analysis using these two complimentary techniques to examine the relationship between the microstructure and optical properties of any features found in epitaxially grown 4H-SiC. Furthermore, this detailed optical analysis provides a pathway for the fundamental understanding of the impact of defects on 4H-SiC device performance and provides a better understanding of their formation and development during epitaxial growth. Indeed, this study suggests that a thorough characterization of defects in 4H-SiC epilayers is necessary in order to correlate and correctly attribute their nature to their impact on electrical performance. If the defect is correctly identified, parameters such as yield, on-state resistance, MOSFETs transfer characteristics (V_{DS}, I_D, V_{GS}), detrimental changes due to REDG evolution, leakage current, and reduction in voltage breakdown can be calibrated and correlated to its nature. These parameters can then be entered in commercial deep learning tools to better sort through devices. 3C-inclusions are present in state-of-the-art commercial 4H-SiC epilayers and all have the same morphological features. Which is to say, a down-fall particle at the interface substrate/epilayer causes strain during the epitaxial growth and results in a high density of dislocations, misoriented 4H-SiC, 3C-polytype, and surrounding stacking faults bounded by partial dislocations. Therefore, this multiscale luminescence analysis is also representative of other 3C-inclusions. In this work, an inclusion was selected as an example, but this method applies to any heterostructures or areas that show BPDs.

ACKNOWLEDGMENTS

This work was authored in part by the National Renewable Energy Laboratory, operated by Alliance for Sustainable Energy, LLC, for the U.S. Department of Energy (DOE) under Contract No. DE-AC36-08GO28308. Funding was provided by the U.S. Department of Energy Advanced Manufacturing Office. The views expressed in the article do not necessarily represent the views of the DOE or the U.S. Government. The U.S. Government retains and the publisher, by accepting the article for publication, acknowledges that the U.S. Government retains a nonexclusive, paid-up, irrevocable, worldwide license to publish or reproduce the published form of this work, or allow others to do so, for U.S. Government purposes.

AUTHOR DECLARATIONS

Conflict of Interest

The authors have no conflicts to disclose.

DATA AVAILABILITY

The data that support the findings of this study are available from the corresponding author upon reasonable request.

REFERENCES

[1]H. Tamaso, K. Sawada, K. Fujikawa, S. Harada, J. Shinkai, H. Tokuda, T. Masuda, M. Honaga, S. Itoh, T. Tsuno, and Y. Namikawa, SEI Tech. Rev. **43** (2008), ISSN ID: 13434349.
[2]L. Lilja, "4H-SiC epitaxy investigating carrier lifetime and substrate off-axis dependence," Doctoral dissertation (Linköping University, 2018).
[3]K. X. Liu, R. E. Stahlbush, M. E. Twigg, J. D. Caldwell, E. R. Glaser, K. D. Hobart, and F. J. Kub, J. Electron. Mater. **36**, 297 (2007).
[4]N. Hoshino, I. Kamata, T. Kanda, Y. Tokuda, H. Kuno, and H. Tsuchida, Appl. Phys. Express **13**, 095502 (2020).
[5]K. Maeda, K. Suzuki, and M. Ichihara, Microsc. Microanal. Microstruct. **4**, 211 (1993).
[6]N. Thierry-Jebali, C. Kawahara, T. Miyazawa, H. Tsuchida, and T. Kimoto, AIP Adv. **5**, 037121 (2015).
[7]Z. Z. Wang, Z. L. Wu, M. M. Ge, H. Q. Bao, Z. F. Ma, and J. Wu, Mater. Sci. Forum **954**, 46 (2019).
[8]B. Chen, H. Matsuhata, T. Sekiguchi, K. Ichinoseki, and H. Okumura, Acta Mater. **60**, 51 (2012).
[9]T. Rana, "High quality silicon carbide epitaxial growth by novel fluorosilane gas chemistry for next generation high power electronics," Doctoral dissertation (University of South Carolina–Columbia, 2013).
[10]X. Zhang, L. Li, M. Skowronski, J. J. Sumakeris, M. J. Paisley, and M. J. O'Loughlin, J. Appl. Phys. **105**, 123529 (2009).
[11]K. Masumoto, K. Kojima, and H. Yamaguchi, Materials **13**, 4818 (2020).
[12]T. Kimoto, A. Iijima, H. Tsuchida, T. Miyazawa, T. Tawara, A. Otsuki, T. Kato, and Y. Yonezawa, in *IEEE International Reliability Physics Symposium Proceedings* (IEEE International Reliability Physics Symposium Proceedings, 2017), p. 2A1.1.
[13]C. Hallin, A. O. Konstantinov, B. Pécz, O. Kordina, and E. Janzén, Diamond Relat. Mater. **6**, 1297 (1997).
[14]S. I. Maximenko, J. A. Freitas, Y. N. Picard, P. B. Klein, R. L. Myers-Ward, K. K. Lew, P. G. Muzykov, D. K. Gaskill, C. R. Eddy, and T. S. Sudarshan, Mater. Sci. Forum **645–648**, 211 (2010).
[15]E. B. Yakimov, G. Regula, and B. Pichaud, J. Appl. Phys. **114**, 084903 (2013).
[16]R. Hirano, Y. Sato, H. Tsuchida, M. Tajima, K. M. Itoh, and K. Maeda, Appl. Phys. Express **5**, 091302 (2012).
[17]R. E. Stahlbush, B. L. Vanmil, R. L. Myers-Ward, K. K. Lew, D. K. Gaskill, and C. R. Eddy, Appl. Phys. Lett. **94**, 041916 (2009).
[18]Y. Miyano, R. Asafuji, S. Yagi, Y. Hijikata, and H. Yaguchi, AIP Adv. **5**, 127116 (2015).
[19]I. Kamata, X. Zhang, and H. Tsuchida, Appl. Phys. Lett. **97**, 172107 (2010).
[20]I. Kamata, X. Zhang, and H. Tsuchida, Mater. Sci. Forum **679–680**, 310 (2011).
[21]R. E. Stahlbush, N. A. Mahadik, and M. J. O'Loughlin, Mater. Sci. Forum **778–780**, 309 (2014).